



Structural Rearrangements That Govern Flow in Colloidal Glasses

Peter Schall, *et al.*

Science **318**, 1895 (2007);

DOI: 10.1126/science.1149308

The following resources related to this article are available online at www.sciencemag.org (this information is current as of January 3, 2008):

Updated information and services, including high-resolution figures, can be found in the online version of this article at:

<http://www.sciencemag.org/cgi/content/full/318/5858/1895>

A list of selected additional articles on the Science Web sites **related to this article** can be found at:

<http://www.sciencemag.org/cgi/content/full/318/5858/1895#related-content>

This article **cites 23 articles**, 3 of which can be accessed for free:

<http://www.sciencemag.org/cgi/content/full/318/5858/1895#otherarticles>

This article appears in the following **subject collections**:

Materials Science

http://www.sciencemag.org/cgi/collection/mat_sci

Information about obtaining **reprints** of this article or about obtaining **permission to reproduce this article** in whole or in part can be found at:

<http://www.sciencemag.org/about/permissions.dtl>

which are as-recorded); this plot reveals a positive correlation between strength and stiffness.

The implication of the correlation between strengths and stiffnesses is that although the fiber samples we created have defects at random intervals on the millimeter scale along the gauge length, these flaws do not have the nature of a stress raiser in a brittle fiber, which would be expected to reduce strength but to have little or no effect on stiffness. It is much more likely that these defects are associated with local deficiencies in densification, which would preclude successful stress transfer by shear between some of the bundles of nanotubes. Consequently, in some sections of the fiber, not all of the nanotube bundles carry an equal share of the load, resulting in both lower fracture strength and decreased stiffness. We believe that these defects are associated with included carbonaceous particles (fig. S3), which induce failure in interbundle stress transfer over much greater distances along the fiber than that occupied by the particle alone. Such particles are seen microscopically with a frequency that is consistent with their distribution at millimeter-scale spacings along the fiber. The strengths reported here represent a measure of success in reducing the level of such included particles, and we expect further levels of process refinement to enable the realization of such high strengths over much longer fibers.

Figure 4A (and table S1) set the strength and stiffnesses of our fibers in the context of a range of mechanical data from commercially available high-performance fibers, as well as reports of properties of other carbon nanotube fibers in the recent literature. The strains shown, and thus the stiffness and energy absorbed up to fracture (table

S1), have been corrected for grip strain. Under laboratory conditions, higher strengths than those guaranteed in a commercial product are sometimes seen. Two reported strengths from laboratory fiber work, one for high-strength polyethylene (24) and one for poly(*p*-phenylene-2,6-benzobisoxazole) (PBO) (25), are plotted as horizontal lines in Fig. 4A. Table S1 also sets the measurements of energy absorbed at fracture (toughness) in the context of other fibers. In Fig. 4B, the performance of our fiber is compared with values reported in the literature for carbon nanotube fibers made by different methods. As some laboratories have not recorded the density of their fibers, we have made this comparison in terms of strength and stiffness rather than specific strength and specific stiffness. One consequence of using these (nonspecific or direct) units is that the estimated error of our measurements is slightly increased.

References and Notes

- M. F. Yu, B. S. Files, S. Arepalli, R. S. Ruoff, *Phys. Rev. Lett.* **84**, 5552 (2000).
- M. M. J. Treacy, T. W. Ebbesen, J. M. Gibson, *Nature* **381**, 678 (1996).
- B. G. Demczyk *et al.*, *Mat. Sci. Eng. A* **334**, 173 (2002).
- T. Dumitrica, M. Hua, B. I. Yakobson, *Proc. Natl. Acad. Sci. U.S.A.* **103**, 6105 (2006).
- T. Belytschko, S. P. Xiao, G. C. Schatz, R. S. Ruoff, *Phys. Rev. B* **65**, 235430 (2002).
- T. Natsuki, K. Tantrakarn, M. Endo, *Carbon* **42**, 39 (2004).
- L. M. Ericson *et al.*, *Science* **305**, 1447 (2004).
- K. L. Jiang, Q. Q. Li, S. S. Fan, *Nature* **419**, 801 (2002).
- M. Zhang, K. R. Atkinson, R. H. Baughman, *Science* **306**, 1358 (2004).
- Y.-L. Li, I. A. Kinloch, A. H. Windle, *Science* **304**, 276 (2004); published online 11 March 2004 (10.1126/science.1094982).

- See supporting material on Science Online.
- X. Zhang *et al.*, *Small* **3**, 244 (2007).
- Q. W. Li *et al.*, *Adv. Mater.* **18**, 3160 (2006).
- M. Motta, A. Moiala, I. A. Kinloch, A. H. Windle, *Adv. Mater.* **19**, 3721 (2007).
- B. Vigolo *et al.*, *Science* **290**, 1331 (2000).
- We express stress as GPa divided by 5G, a unit known as specific stress in materials science that is exactly numerically equivalent to newtons per tex.
- I. M. Ward, Ed., *Structure and Properties of Oriented Polymers* (Halsted/Wiley, New York, 1975).
- T. Liu, S. Kumar, *Nano Lett.* **3**, 647 (2003).
- T. Amornsakchai, D. L. M. Cansfield, S. A. Jawad, G. Pollard, I. M. Ward, *J. Mater. Sci.* **28**, 1689 (1993).
- I. M. Ward, in *Solid Phase Processing of Polymers*, I. M. Ward, P. D. Coates, M. M. Dumoulin, Eds. (Hanser Gardner, Munich, 2000), p. 133.
- N. Lissart, J. Lamon, *J. Mater. Sci.* **32**, 6107 (1997).
- R. D. Maurer, Ed., *Strength of Inorganic Glass* (Plenum, New York, 1985).
- J. D. H. Hughes, H. Morley, E. E. Jackson, *J. Phys. D* **13**, 921 (1980).
- H. van der Werff, A. J. Pennings, *Colloid Polym. Sci.* **269**, 747 (1991).
- W. A. Adams, personal communication.
- Supported by Consejo Nacional de Ciencia y Tecnología (Mexico), the Engineering and Physical Sciences Research Council (UK), and the U.S. Army International Technology Center–Atlantic. We thank S. Fraser for valuable comments and M. Pick for his considerable technical contribution to this research.

Supporting Online Material

www.sciencemag.org/cgi/content/full/1147635/DC1
Materials and Methods

Figs. S1 to S3

Table S1

Movie S1

References

11 July 2007; accepted 2 November 2007

Published online 15 November 2007;

10.1126/science.1147635

Include this information when citing this paper.

Structural Rearrangements That Govern Flow in Colloidal Glasses

Peter Schall,^{1,2*} David A. Weitz,^{2,3} Frans Spaepen²

Structural rearrangements are an essential property of atomic and molecular glasses; they are critical in controlling resistance to flow and are central to the evolution of many properties of glasses, such as their heat capacity and dielectric constant. Despite their importance, these rearrangements cannot directly be visualized in atomic glasses. We used a colloidal glass to obtain direct three-dimensional images of thermally induced structural rearrangements in the presence of an applied shear. We identified localized irreversible shear transformation zones and determined their formation energy and topology. A transformation favored successive ones in its vicinity. Using continuum models, we elucidated the interplay between applied strain and thermal fluctuations that governs the formation of these zones in both colloidal and molecular glasses.

The hallmark of any glass is a very low atomic or molecular mobility within a disordered solid, many orders of magnitude smaller than that of a fluid. This mobility is a result of thermally induced structural rearrangements, which typically occur at a very low rate. Structural rearrangements must also occur as a response of the glass to an externally

applied shear; this causes a directional bias in the structural rearrangements that produces the macroscopic strain (1). Because the glass structure is so highly constrained, these structural rearrangements must entail reorganization of the constituent molecular units over some larger length scale (2). Nevertheless, in molecular glasses, these length scales are still too

small and the time scales are too short for direct observation. The only direct evidence for the existence of local shear transformation zones that produce macroscopic strain comes from bubble raft experiments (3) and computer simulations of two-dimensional (4–6) and three-dimensional (3D) glasses (7–10). Direct real-space visualization of structural rearrangements can be made in suspensions of colloidal particles as they can be quenched into a glassy state by rapid densification of the particles from a fluid state (11, 12). These systems lose ergodicity due to crowding at high particle volume fraction, ϕ , leading to a transition to a glassy state at $\phi_g \approx 0.58$ (13). Experiments and simulations suggest that when ϕ_g is approached from the fluid phase, particle rearrangements occur cooperatively on increasing length scales (2, 14, 15). For $\phi > \phi_g$, such rearrangements are

¹Van der Waals-Zeeman Institute, University of Amsterdam, Valckenierstraat 65, 1018 XE Amsterdam, Netherlands. ²Harvard School of Engineering and Applied Sciences, Cambridge, MA 02138, USA. ³Department of Physics, Harvard University, Cambridge, MA 02138, USA.

*To whom correspondence should be addressed. E-mail: pschall@science.uva.nl

highly constrained (15). Nevertheless, thermally induced aging, often called “structural relaxation,” occurs (13, 16) and must entail some form of cooperative motion.

We visualize structural rearrangements in colloidal glasses in three dimensions and in real time by following the microscopic strain distribution under shear. We identify the shear transformation zones and show that they have a spatial extent of a few particle diameters and involve a highly localized structural rearrangement that results in a strain of ~ 0.1 immediately in the vicinity of the central particle. We determine their activation energy, $E^* \sim 16 k_B T$, where $k_B T$ is the thermal energy; thus, they can be induced by thermal fluctuations. They also can be induced through application of very small shears. Moreover, the elasticity of the glass results in coupling between the transformation zones, which, upon increasing strain, leads to a network of transformation zones that extends across the sample.

We prepared a 42- μm -thick colloidal glass by quenching silica spheres with a diameter of 1.5 μm and a polydispersity of 3.5% (17) from a dilute suspension onto a coverslip by centrifugation to a volume fraction of roughly 0.61, well into the colloidal glassy state. Because the density of the silica spheres is greater than that of the solvent, ϕ increases with sample depth. The sample is sufficiently deep into the glassy state that crystallization is not observed. Boundary-

induced crystallization is suppressed by a layer of polydisperse spheres sintered onto the coverslip. The silica particles are suspended in a mixture of water and dimethylsulfoxide, which matches their refractive index. We added a small amount of fluorescein to the solvent so that under fluorescent imaging, particles appear as dark spots on a bright background. We carefully introduced a fine metal grid (18) from above to fix the top of the sediment, and we used a piezoelectric translation stage to move the coverslip to apply shear at very small rates of $\sim 10^{-5} \text{ s}^{-1}$. We used confocal microscopy to image individual particles in a 47 μm by 50 μm by 23 μm volume and determined their positions in 3D with an accuracy of 0.03 μm in the horizontal and 0.05 μm in the vertical direction (15). We tracked the motion of individual particles for the 60-min duration of each experiment by acquiring 3D image stacks every 150 s; each image stack took 60 s to acquire.

Structural rearrangements can be thermally activated even in the absence of shear. We follow particle trajectories in an unsheared glass for 20 min and identify the nearest neighbors of each particle as those separated by less than r_0 , the first minimum of the pair correlation function. To calculate the time-dependent strain, we determine the symmetric part of the best affine deformation tensor that transforms the change of the nearest-neighbor vectors over the time interval (6), and we smooth the results by averaging over nearest neighbors (19, 20). The x , y , and z directions are

chosen along the edges of the imaged volume (Fig. 1A). We focus on the shear component ϵ_{yz} of the strain tensor and illustrate its value for two subsequent 2.5-min intervals in 3- μm -thick sections at $z = 13.5 \mu\text{m}$ in Fig. 1, B and C. Red and blue spheres indicate regions with positive and negative shear strain, respectively. Regions of strain extending over many particles are evident (arrows). Furthermore, by comparing red and blue regions, we find that localized regions of large strain reverse their sign in subsequent images as highlighted by the arrows in Fig. 1, B and C. We interpret these strain oscillations as thermal fluctuations. To check this hypothesis, we calculate the elastic energies associated with the shear strain distribution and determine the relative frequency of the energies. We divide the volume into cubes of size $a = 3 \mu\text{m}$, so that each cell contains about nine particles, roughly equal to the number of nearest neighbors. The magnitude of ϵ_{yz} calculated for cells centered at $z = 13.5 \mu\text{m}$ and for the second time interval (Fig. 1C) is plotted in Fig. 1D (21). We calculate the elastic energy in each cell, $E/\mu = (1/2)(2\epsilon_{yz}^2)a^3$, where we have normalized by the shear modulus, μ . The probability distribution of the normalized energies is well described by an exponential as expected for a thermally equilibrated system, as shown in Fig. 1E. Because $\ln f(E) = -\mu(E/\mu k_B T)$, we obtain the shear modulus, $\mu = 0.056 \text{ Pa}$, from the fit, indicated by the straight line in Fig. 1E. This value is consistent with $\mu = 0.1 \text{ Pa}$,

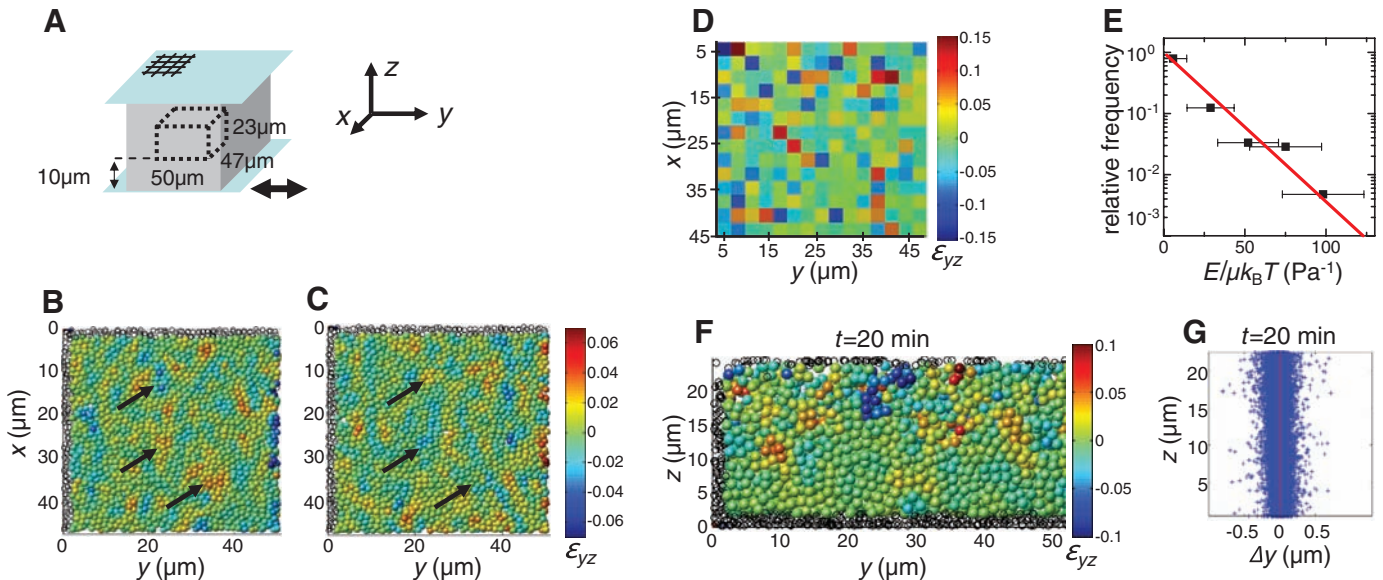


Fig. 1. Thermally induced strain fluctuations (A) Schematic showing the colloidal glass (gray), and the bottom coverslip and top grid (blue) with respect to the 47 μm by 50 μm by 23 μm section depicted in (B) to (D) and (F). (B to F) Strain fluctuations in the unsheared glass. Color in (B) to (D) and (F) indicates the value of the local shear strain, ϵ_{yz} (see color scale). (B and C) x - y sections (3 μm thick) at $z = 13.5 \mu\text{m}$, showing the distribution of the incremental shear strain during two consecutive 2.5-min intervals. Arrows mark regions in which the strain changes sign from (B) to (C). (D) Array of 3 μm by 3 μm squares, showing values of the incremental shear strain in 3 μm by 3 μm by 3 μm cells at $z = 13.5 \mu\text{m}$ for the section shown in (C). Each cell contains roughly nine particles. (E) Distribution of normalized strain energies,

$E/\mu k_B T$, calculated from the strain values depicted in (D). Squares at $E/\mu k_B T = 23n \text{ Pa}^{-1}$ with $n = 0, 1, 2, \dots$ indicate the relative frequency of energy values in intervals $[23n, 23(n + 1)] \text{ Pa}^{-1}$. Horizontal bars indicate the uncertainty in energy associated with the uncertainty in strain due to the limited accuracy in particle positioning. We assume that the measured particle coordinates have a Gaussian distribution of width 0.03 μm in the x and y direction, and 0.05 μm in the z direction, around the real positions. The red line has a slope of -0.056 Pa . (F) y - z section (8 μm thick) centered at $x = 14 \mu\text{m}$ showing the cumulative shear strain at $t = 20 \text{ min}$. Red and blue regions persist at even later times. (G) Cumulative displacements, Δy , from $t = 0$ to $t = 20 \text{ min}$ of particles (+) at height between $z = 0$ and $z = 23 \mu\text{m}$.

measured for crystals of similar thickness and made of the same particles (22). Similar oscillations exist for all components of strain, both shear and uniaxial. This supports our hypothesis that the strain oscillations are indeed caused by thermal fluctuations.

Thermal fluctuations can also induce irreversible rearrangements. To probe these, we determine the cumulative strain that occurs during the entire 20-min interval. We plot a reconstruction of an 8- μm -thick section in the yz plane centered at $x = 14 \mu\text{m}$ in Fig. 1F. Localized regions with strain amplitudes even larger than those of the strain fluctuations have developed, and we confirm that these regions persist at longer times. These structural rearrangements do not, however, lead to macroscopic strain as confirmed by the plot of the z coordinates of the individual particles as a function of their cumulative displacements in the y direction; no shear gradient is observed, as shown in Fig. 1G.

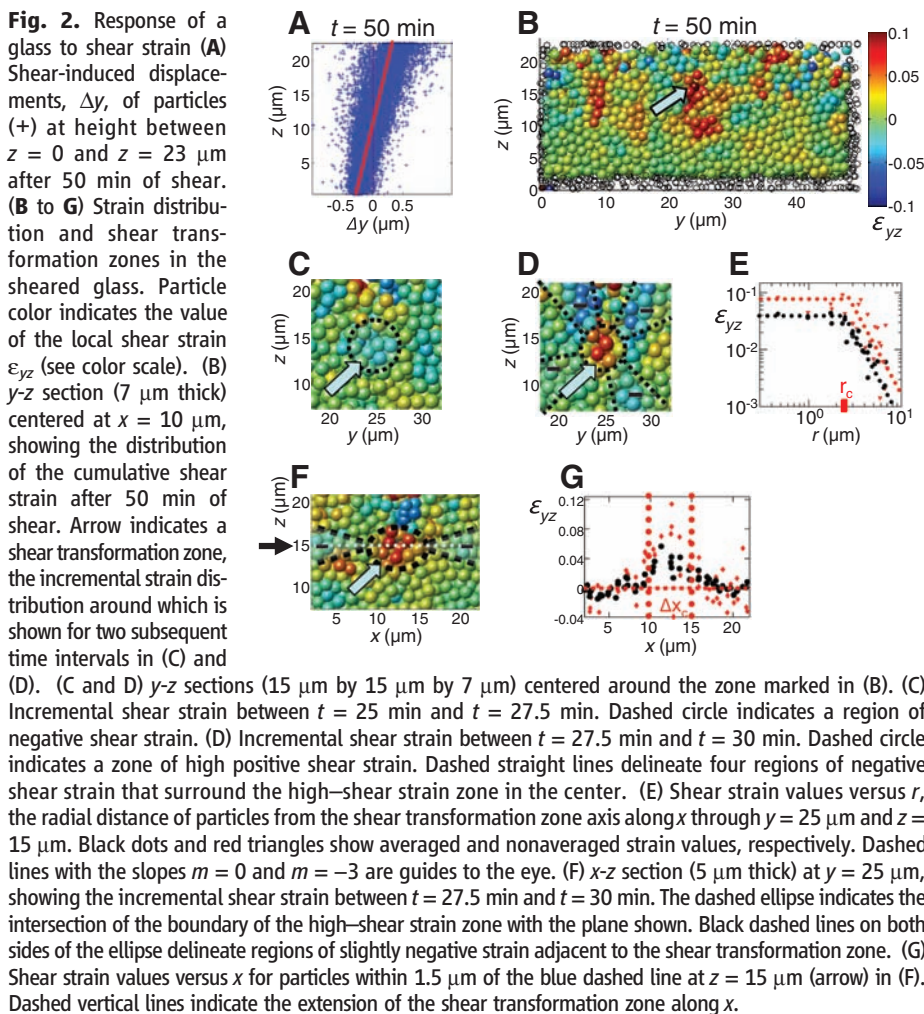
To investigate these structural rearrangements more closely, we study their behavior upon application of shear. We apply positive shear strain by displacing the bottom coverslip in the negative y direction while keeping the top plate at a fixed position. We find that the mean Δy in-

creases almost linearly with z corresponding to a nearly uniform shear strain, as shown by the plot of the z coordinates of all particles as a function of their y displacements in Fig. 2A. The slight curvature of the data indicates a somewhat reduced shear strain at small z . We attribute this to the higher density at the bottom of the sediment. We determine the macroscopic shear strain, γ , from the difference of the mean of the Δy distributions across the full sample height $\Delta z = 23 \mu\text{m}$ (slope of the red line). We obtain $\gamma = 0.03$ for the 50-min time interval, which corresponds to an average strain rate of 10^{-5} s^{-1} .

We can again identify localized regions of structural rearrangements, but now induced by the applied strain. We show the cumulative strain ϵ_{yz} in a 7- μm -thick section at $x = 10 \mu\text{m}$ in Fig. 2B. Red spheres indicate local shear strain in the direction of the applied shear, whereas blue spheres indicate shear strain opposite to the applied strain. The shear strain is not distributed homogeneously, but is instead localized as shown by the zones of concentrated red spheres. These regions are typically a few particle diameters wide. We focus on an individual region (arrow) and investigate the strain distribution when it is first formed. A large portion of the strain occurs

in one time step, which allows us to identify its formation. Reconstructions centered on this region with adjacent frames measured just before and just after its formation are shown in Fig. 2, C and D. The red spheres in Fig. 2D (arrow) indicate high local shear strain associated with the formation of the shear transformation zone. We find that before the zone is formed, opposite strain concentrates in the same region (blue spheres in Fig. 2C). This suggests that the formation of the zone is caused by a thermally induced strain fluctuation. During the time step in which the shear transformation zone is formed, four zones of negative shear strain (–) surround the center region shown by red in Fig. 2D. This fourfold symmetric strain distribution is characteristic of the distortion of an elastic matrix around a volume that undergoes a shear transformation (23). We determine the magnitude of ϵ_{yz} as a function of distance, r , from the shear transformation zone center, by plotting the strain values of all particles in the lower left sector of a cylinder centered at $y = 25 \mu\text{m}$ and $z = 15 \mu\text{m}$ as a function of their distance from the cylinder axis (Fig. 2E). Black dots show the averaged strain values depicted in Fig. 2D, whereas the red triangles represent values of ϵ_{yz} that have not been averaged over nearest neighbors. The averaged values are significantly smaller, which we attribute to the truncation of the strain magnitude that results from the averaging; we use the nonaveraged strain values for further calculations. The shear strain is constant at small r , and decays as r^{-3} at larger r (dashed lines in Fig. 2E), as expected for the strain field around a volume that undergoes a shear transformation (23). The crossover defines the radius of the core of the shear transformation zone, $r_c = 2.3 \mu\text{m}$, which is roughly equal to three particle radii. To explore the strain distribution in the third direction, we show a 5- μm -thick section along the xz plane that contains the same shear transformation zone in Fig. 2F. The core of the zone is elongated along the x direction, bounded by regions of slightly negative strain. To determine its extent in x , we consider particles within 1.5 μm of the dotted line, which goes through the center of the zone, and plot their ϵ_{yz} as a function of x in Fig. 2G. We observe a maximum of $\epsilon_0 \approx 0.08$ centered between $x = 10 \mu\text{m}$ and $x = 15 \mu\text{m}$ with a crossover to negative strain values on either side. Thus, we take the width of the core of the shear transformation zone to be $\Delta x_c = 5 \mu\text{m}$.

We calculate the energy cost, E_f , and activation volume, $V^* = k_B T \ln \dot{\gamma} / \dot{\tau}$, where $\dot{\gamma}$ is the macroscopic shear rate and τ the applied stress, associated with the formation of the shear transformation zone using a continuum-elastic model. We first determine the strain field of an elastic matrix around a spherical inclusion of radius r_c that undergoes a uniform shear transformation of ϵ_0 (24). We calculate the total elastic strain energy inside and outside the inclusion by integrating the total energy density $w = (1/2)(2\mu\epsilon_{ij}^2 + \lambda\epsilon_{kk}^2)$ (25) over the volume. We



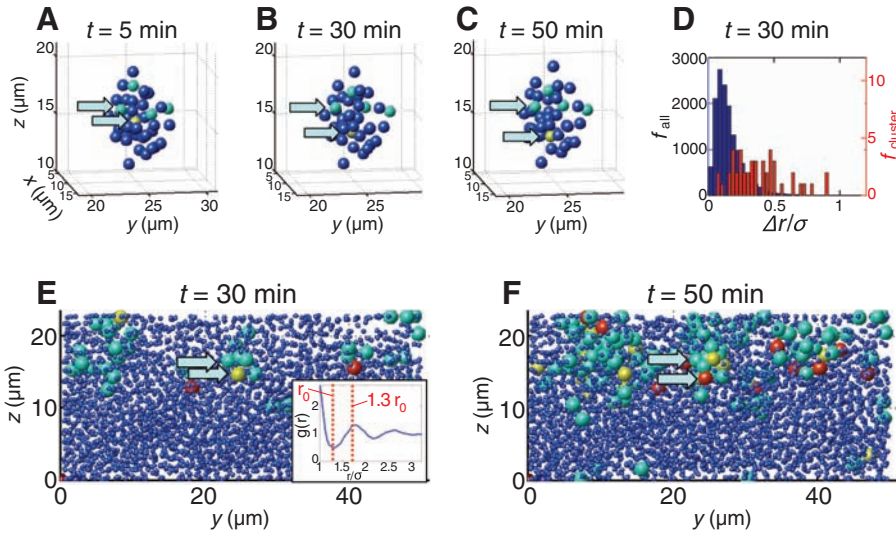


Fig. 3. Structural rearrangements at the particle scale. (A to C) Reconstructed images showing particle arrangements within the shear transformation zone of Fig. 2, B to G, at $t = 5, 30,$ and 50 min. Arrows mark one yellow and four green particles, which are nearest neighbors at $t = 5$ min and become separated at later times. (D) Histograms showing the normalized particle displacements, $\Delta r/\sigma$, where σ is the particle radius, at $t = 30$ min, for shear transformation zone particles (red bars, right scale) and for all particles outside the shear transformation zone (blue bars, left scale). Particles within the shear transformation zone exhibit many more large displacements. (E and F) Reconstruction of a $10\text{-}\mu\text{m}$ -thick glass section centered at $x = 7\ \mu\text{m}$ shows nearest-neighbor changes in the sheared glass at $t = 30$ min and $t = 50$ min. Large green, yellow, and red spheres indicate particles that lose one, two, and three nearest neighbors, respectively. All other particles are drawn as smaller spheres for clarity. Nearest-neighbor changes occur in high-shear strain regions (compare to Fig. 2B). Arrows indicate the same particles as marked in (A) to (C). The inset in (E) shows the radial distribution function, $g(r)$, of the glass used for identifying nearest neighbors at $t = 0$. Particles with distances smaller than r_0 (left dashed line) are nearest neighbors; all particles that move farther away than $1.3r_0$ from their nearest neighbor (right dashed line) are defined as having lost their neighbor.

approximate the Lamé constant λ by $2\nu\mu/(1 - 2\nu)$ using the Poisson ratio $\nu = 1/3$ and obtain $E_f' = 18.9 k_B T$. We calculate the activation volume by integrating the distribution of the technical shear strain $\gamma = 2\varepsilon_{yz}$ over the volume and obtain $V^{*'} = 6.9\ \mu\text{m}^3$. We correct E_f' and V^{*}' for the ellipsoidal shape of the shear transformation zone by multiplying by $\Delta x_c/2r_c$ and obtain $E_f = 20.5 k_B T$ and $V^* = 7.5\ \mu\text{m}^3$. We determine the volume of a particle, $V_0 = 1.88\ \mu\text{m}^3$, from the peak of the pair correlation function at $1.53\ \mu\text{m}$; thus, the activation volume is roughly four particle volumes. Interestingly, this value is of the same order as those for metallic glasses determined from measurements of the stress dependence of the strain rate; for example, for a PdNiCuP alloy, V^* is about eight atomic volumes (26).

Because the rearrangements in the shear transformation zones contribute to plastic flow, they must be irreversible and persist after they have been created. To check this, we reversed the shear direction and confirmed that the shear transformation zones that we investigated here do not reverse but remain locked in their sheared configurations (27). To elucidate this irreversibility, we investigated the structural rearrangements on the single-particle level in the core of the shear transformation zone. We show reconstructions of the arrangement of particles in the shear transformation zone core at $t = 5, 30,$ and 50 min in Fig. 3, A to C. We highlight a particle in the zone center (yellow sphere), which exhibits a large displacement downward and thereby loses some of its nearest neighbors (green spheres). To quantify the particle displacements in this zone, we determined the displacement of the particles relative to the average displacement of particles at the same height, $\Delta r = [(\Delta x - \langle \Delta x \rangle)^2 + (\Delta y - \langle \Delta y \rangle)^2 + (\Delta z - \langle \Delta z \rangle)^2]^{0.5}$. We plot the distribution of Δr at $t = 30$ min in Fig. 3D. The magnitudes of the displacements of particles in the shear transformation zone (red bars) are significantly larger than those of the particles outside the zone

Table 1. Activation parameters of individual shear transformation zones. Activation volume V^* , energy of formation E_f , and activation energy $E^* = E_f - \tau V^*$ of shear transformations were determined from the individual incremental strain distributions associated with the formation of the transformations. The shear stress τ was taken to be $\tau = \gamma_0 \mu$ with $\gamma_0 = 0.012$, the macroscopic shear strain at formation of the first shear transformation, and the shear modulus $\mu = 0.056$ Pa (Fig. 1E). The particle volume V_0 is $1.88\ \mu\text{m}^3$.

V^*/V_0	E_f ($k_B T$)	E^* ($k_B T$)
4.0	20.5	19.2
4.6	19.3	17.8
3.6	13.9	12.7
3.7	16.5	15.3
3.4	16.5	15.4
3.8	19.6	18.4

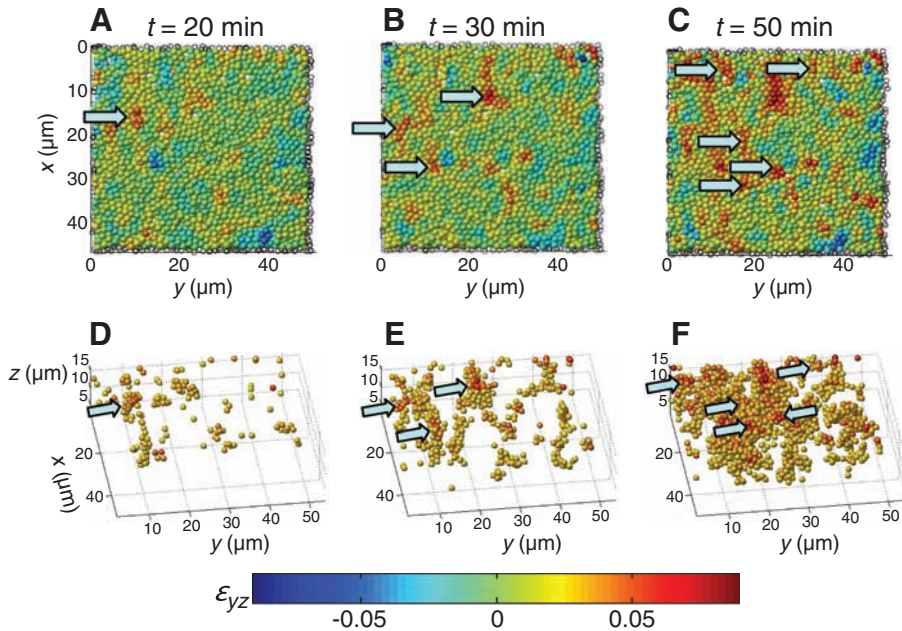


Fig. 4. Strain evolution during shear. Distribution of the cumulative shear strain after 20, 30, and 50 min of shear. For each frame, arrows indicate shear transformation zones that have been formed in the time interval before the frame shown. Shear transformation zones appear to form a connected network at $t = 50$ min. (A to C) x - y sections ($5\ \mu\text{m}$ thick) centered at $z = 13.5\ \mu\text{m}$. (D to F) Perspective view of $16\text{-}\mu\text{m}$ -thick sections showing particles with shear strain values larger than 0.025 only.

(blue bars). Two particles in the shear transformation zone move almost as much as their radius; one of these is the yellow sphere in Fig. 3, A to C. Such large displacements of isolated particles cause notable changes in their nearest-neighbor configuration, as illustrated by the motion of the yellow sphere. This causes the irreversibility of the shear transformation. To characterize this irreversibility, we identify all particles that lose one or more nearest neighbors, where we define loss of a nearest neighbor to occur when that particle moves farther away than βr_0 , where we arbitrarily choose $\beta = 1.3$, as shown in the inset of Fig. 3E. We show these particles in a 10- μm -thick slice in the yz plane at two different times in Fig. 3, E and F; large green, yellow, and red spheres illustrate particles that have lost one, two, and three nearest neighbors, respectively. These spheres concentrate in regions, which grow with time and coincide with the zones that exhibit high shear strain (Fig. 2B). This supports our interpretation that shear transformations are irreversible: The nearest-neighbor changes lead to new particle configurations, stabilizing the transformed zone.

The existence of these shear transformation zones indicates that locally, the strain is highly concentrated. The long-range strain field of a shear transformation may facilitate the nucleation of another shear transformation zone in its vicinity: The formation of new zones may be spatially and temporally correlated. To explore this possibility, we follow the evolution of the ϵ_{yz} distribution over the entire duration of the experiment. To smooth the thermally induced strain fluctuations, we average the particle positions over two adjacent frames and calculate the time-averaged shear strain, ϵ_{yz}^* . We show the evolution of the ϵ_{yz}^* distribution in Fig. 4. A 5- μm -thick section in the xy plane centered at $z = 13.5 \mu\text{m}$ is shown in Fig. 4, A to C. Three-dimensional reconstructions of a thicker slice, 16 μm in height, depicting only particles with $\epsilon_{yz}^* > 0.025$, are shown in Fig. 4, D to F. The number of shear transformation zones increases with strain; new zones appear, while existing ones persist. The images show that a shear transformation zone induces new ones in its vicinity. For example, the zone formed at the earliest time (arrows in Fig. 4, A and D) induces the formation of three adjacent zones (arrows in Fig. 4, B and E), each of which again induces additional adjacent zones (Fig. 4, C and F). That this coupling results from the long-range strain fields is corroborated by the observation that branches of positive strain develop between the individual shear transformation zones, as shown by the more yellow-colored particles between the zones. These branches connect the individual shear transformation zones into a network, which ultimately permeates the entire field of view at 50 min (Fig. 4F).

Even though the applied strain helps induce these shear transformation zones, they are nevertheless still predominantly thermally activated. We can understand this by comparing the

energy induced by the applied shear with the energy of formation of the shear transformation zone. The external work due to the applied shear stress τ is τV^* . We estimate the shear stress to be constant once the sample has exceeded the macroscopic yield strain, where the first shear transformation occurs, $\gamma_0 = 0.012$; thus, we take $\tau = \gamma_0 \mu$. We calculate the activation volumes, V^*_i , from the individual strain distributions of several shear transformation zones and list them in Table 1. Because the average activation volume is $V^*_{av} = 3.8 V_0$, the typical work due to shear is $\sim 1 k_B T$. By comparison, we calculate the formation energy of the same shear transformation zones (Table 1). Although there is some variation, their typical value is $E_f = 18 k_B T$, significantly larger than the work done by the applied shear. Thus, the shear transformation zones are thermally activated with an activation energy of $E^*_i = E_{f,i} - \tau V^*_i$, and we also list these values in Table 1.

The average activation energy is $E^*_{av} = 16.5 k_B T$; this should be compared with the measured value of E^* determined from the rate, J , at which shear transformation zones are induced. We use $J = f_0 m \exp(-E^*/k_B T)$, where $m = 3400$ is the total number of particles, and $f_0 = 100 \text{ s}^{-1}$ is a characteristic frequency of the particles determined by their diffusion time between nearest-neighbor particles (20). We determine $J = 3 \times 10^{-3} \text{ s}^{-1}$ from the total number of shear transformation zones observed during the 50-min interval in the 5- μm -thick section; thus, $E^* = 18.5 k_B T$, in very good agreement with E^*_{av} determined from the strain distributions.

These results highlight the role of the shear transformation zone in the flow of glasses. The structural rearrangements are thermally activated and are highly localized. Although these results are obtained on colloidal glasses, similar behavior should occur in metallic and molecular glasses. Application of the measured strain distribution on the atomic scale to a metallic glass with $\mu \sim 30 \text{ GPa}$ (28) yields a shear-zone energy close to that found for our colloidal glass. Although activation energies determined from isoconfigurational viscosity measurements on metallic glasses at 600 K are roughly four times as large as this value (29), the ratio of the activation energy to the thermal energy is only a factor of 2 larger than in our colloidal system. This reflects the 10 orders of magnitude higher attempt frequency in metallic glasses at equal nucleation rates. The ratio of the external work τV^* to the thermal energy is of the same order as in typical deformation tests on metallic glasses at the same strain rate (26), which indicates that the effects of thermal fluctuations in our experiment are similar to those in deformation of metallic glasses. Our results also highlight the coupling between shear transformation zones: The long-range elastic stress field of each zone induces new zones in its vicinity, and upon sufficient external strain, these zones extend throughout the volume. A similar coupling between shear transformation zones is expected in atomic and molecular glasses.

References and Notes

1. F. Spaepen, *Acta Metall.* **25**, 407 (1977).
2. G. Adam, J. H. Gibbs, *J. Chem. Phys.* **43**, 139 (1965).
3. A. S. Argon, Y. Kuo, *Mater. Sci. Eng.* **39**, 101 (1979).
4. K. Maeda, S. Takeuchi, *Phys. Status Solidi A* **49**, 685 (1978).
5. C. Maloney, A. Lemaitre, *Phys. Rev. Lett.* **93**, 195501 (2004).
6. M. L. Falk, J. S. Langer, *Phys. Rev. E* **57**, 7192 (1998).
7. S. Kobayashi, K. Maeda, S. Takeuchi, *Acta Metall.* **28**, 1641 (1980).
8. K. Maeda, S. Takeuchi, *Philos. Mag. A* **44**, 643 (1981).
9. D. Srolovitz, V. Vitek, T. Egami, *Acta Metall.* **31**, 335 (1983).
10. A. C. Lund, C. A. Schuh, *Acta Mater.* **51**, 5399 (2003).
11. P. N. Pusey, W. van Meegen, *Nature* **320**, 340 (1986).
12. A. van Blaaderen, P. Wiltzius, *Science* **270**, 1177 (1995).
13. W. van Meegen, T. C. Mortensen, S. R. Williams, J. Müller, *Phys. Rev. E* **58**, 6073 (1998).
14. C. Donati, S. C. Glotzer, P. H. Poole, *Phys. Rev. Lett.* **82**, 5064 (1999).
15. E. R. Weeks, J. C. Crocker, A. C. Levitt, A. Schofield, D. A. Weitz, *Science* **287**, 627 (2000).
16. N. B. Simeonova, W. K. Kegel, *Phys. Rev. Lett.* **93**, 035701 (2004).
17. Micromod, Sicstar, 1.5 μm .
18. SPI supplies, G1000HS, Ni grid, mesh size 25 μm .
19. For each particle with center at $r(t)$, we determine the vectors $d_j(t) = r(t) - r_j(t)$ to all nearest neighbors j at time t . We then compare these vectors with the nearest-neighbor vectors at time $t - \Delta t$, $d_j(t - \Delta t)$. The best affine deformation tensor, α , that transforms the nearest-neighbor vectors at the earlier time, $t - \Delta t$, to the vectors at time t is determined by minimizing the mean square difference, $\sum_j |d_j(t - \Delta t) - \alpha d_j(t)|^2$ (6). The symmetric part of α corresponds to the strain tensor of the particle under consideration. To smooth the resulting strain distribution, we average the strain tensor of each particle with those of its nearest neighbors and assign the resultant average strain tensor to the particle under consideration.
20. P. Schall, I. Cohen, D. A. Weitz, F. Spaepen, *Nature* **440**, 319 (2006).
21. We first find the particle whose center is closest to the center of the cell. For this particle with center at $r(t)$ at time t , we determine the vectors $d_j(t) = r(t) - r_j(t)$ to all other particles j in the cell. We compare these vectors with the interparticle vectors at time $t - \Delta t$, $d_j(t - \Delta t)$. We use the difference between $d_j(t)$ and $d_j(t - \Delta t)$ to calculate the strain tensor by the procedure described in (19).
22. P. Schall, I. Cohen, D. A. Weitz, F. Spaepen, *Science* **305**, 1944 (2004).
23. G. Picard, A. Ajdari, F. Lequeux, L. Bocquet, *Eur. Phys. J. E* **15**, 371 (2004).
24. J. D. Eshelby, *Proc. R. Soc. A* **252**, 561 (1959).
25. L. D. Landau, E. M. Lifshitz, *Theory of Elasticity*, Course of Theoretical Physics, vol. 7 (Elsevier Butterworth-Heinemann, Oxford, ed. 3, 1986).
26. M. Heggen, F. Spaepen, M. Feuerbacher, *J. Appl. Phys.* **97**, 033506 (2005).
27. When shearing back to zero strain, we observe that some shear transformation zones reverse. These may be considered as anelastic. The ones of interest here, however, do not go back.
28. T. Soshiroda, M. Koiki, T. Masumoto, *J. Non-Cryst. Solids* **22**, 173 (1976).
29. A. I. Taub, F. Spaepen, *Acta Metall.* **28**, 1781 (1980).
30. We thank J. Hutchinson for assistance in the calculation of the shear energy around an inclusion and I. Cohen for the use of the shear cell. This work was supported by the Innovational Research Incentives Scheme ("VIDI" grant) of the Netherlands Organization for Scientific Research (NWO) (P.S.) and by the NSF (DMR-0602684) and the Harvard Materials Research and Engineering Center (DMR-0213805).

16 August 2007; accepted 30 October 2007
10.1126/science.1149308